Chemical Science

ROYAL SOCIETY OF CHEMISTRY

EDGE ARTICLE

View Article Online
View Journal

Cite this: DOI: 10.1039/d6sc01492e

All publication charges for this article have been paid for by the Royal Society of Chemistry

Regenerating spent $LiFePO_4$ with tailored molecular groups: from bulk lattice repair to surface conductive coating for enhanced cycling stability

Yi Chen, † Xizhuo Chen,† Zihao Zeng, Wei Sun, Yue Yang and Peng Ge *

Due to its economic and environmental value, the recycling of spent $LiFePO_4$ (S-LFP) has been the subject of plenty of attention. However, it still suffers from inferior energy-storage properties, ascribed to the fact that the fading traits from bulk-phase to surface layers are hardly tailored at the same time. Herein, through the control of the active structure of amino acid, S-LFP is successfully regenerated with optimized Li–Fe anti-sites and high-conductive N-doped double carbon layers. Their internal lattice stress is effectively alleviated, bringing about the removal of phase cracks. Through the balancing between H^+ and electrons cloud of O-atoms, the further dissolution of Fe-ions is inhibited from nano-size solid-solution $LiFePO_4$/$FePO_4$, meanwhile without the formation of by-product Li_3PO_4. The optimized capacity could be maintained at 134 mAh g^{-1} at 1.0C after 500 cycles, with a capacity retention ratio 95.7%. Even at 5.0C, their initial capacity was still kept about ~120 mAh g^{-1} with a capacity retention ratio of 92.2% after 1000 cycles. Supported by the detailed kinetic analysis, the suitable anti-sites and double carbon-layers served important roles for the enhancements of ion-diffusion behaviors and the decrease of internal resistance. More significantly, the uniform chemical–electrochemical interface could be noted after numerous cycles. Given this, the work is expected to illustrate the regeneration effect of molecular groups, whilst providing controllably repairing strategies for S-LFP.

Received 21st February 2026
Accepted 23rd March 2026

DOI: 10.1039/d6sc01492e

rsc.li/chemical-science

Introduction

Along with the wide application of mobile electric devices, the installed capacity of lithium-ion batteries (LIBs) continues to increase. However, restrained by the limited service life (8–10 years), the retired "wave" should be emphasized, due to the rich value-elements and serious potential pollution.[1–3] Lithium iron phosphate ($LiFePO_4$, LFP), as the main member of LIBs cathode, displays high safety and low cost, which has occupied 50% above in the energy-storage market. That is to say, the retired capacity of spent LFP (S-LFP) would be extremely large, which could reach up to 400 000 tons in 2030 as predicted. For suitably treating S-LFP, a series of recycling strategies have been explored, mainly including element-extracting and direct regeneration.[4–6] Compared to the former, the latter offers a shorter process and higher value by recovering the degraded structure. Nowadays, about regeneration manner, it could be divided: solid-phase reconstruction, solvothermal repairing, and electrochemical Li-replenishing.[7,8] Among them, solvothermal manners could be utilized to overcome the issue about non-uniform Li-replenishing, with the further lowering of energy consumption. Based on the previous reports, the reducing agents served important roles in the transformation from Fe^{3+} to Fe^{2+}, such as ascorbic acid, glucose, *etc.*[9–11]

However, the key internal roles of reducing agents are not molecular structures, but about their precise chemical state of active functional groups in the molecular microenvironment, especially for hydroxyl groups (–OH).[12–16] As is known, its reduction potential and acid–base traits are dynamically regulated by its local chemical microenvironment, which could be determined by its positional identity (primary, secondary, tertiary, or phenolic), electronic effects (inductive, conjugative), and the steric bulk of neighboring substituents.[17–21] For instance, –OH groups of isopropanol, attached with an electron-donating alkyl chain, could exhibit high electron density on O-atoms, which leads to the inferior ability for the reduction of Fe^{3+}, and they may serve roles as a base. In contrast, when –OH groups are influenced by adjacent electron-withdrawing groups like carbonyl or nitro groups from lactic and citric acid, the reduced electron density of O-atoms could be noted, along with the facile dissociation of the hydrogen atom and enhanced acidity. Clearly, these traits could induce readily oxidized –OH groups, bringing about interesting reduction pathways and

School of Mineral Processing and Bioengineering, Central South University, Changsha, 410083, China. E-mail: 219122@csu.edu.cn

† These authors contributed to the work equally and should be regarded as co-first authors.

efficiency. Obviously, the spatial positions and branched chain of –OH groups play great roles in their regeneration properties, through the tailoring of thermodynamic and kinetic behaviors. That is to say, at specific hydrothermal temperature and pH conditions, the thermodynamic driving force and reaction rate of $Fe^{3+} \rightarrow Fe^{2+}$ could be regulated through its standard reduction potential and deprotonation constant. According to the previous reports, the function groups of –OH-based reducing agents are not scarcely discussed, always regarded as "black box", especially the relationship between molecular-level structural features of –OH and the regeneration properties.[12,20,21] Moreover, during charge/discharge cycle, the carbon layer of surface would be deteriorated by the shocking of Li-ions and the erosion of electrolyte, resulting in the lowering degree of graphitization.[22] Notably, the inferior carbon layer may result in poor rate capability, accompanied by serious side reactions on the surface. Thus, the regeneration of S-LFP should target not only the bulk structure but also its destroyed surface. As is known, –OH-based organic matter could serve as a carbon resource to form surface coating layers. Given this, exploring suitable OH-based agents would serve significant roles in the high-quality S-LFP regeneration.

Herein, through the control of function groups on the branched chains, S-LFP is successfully upcycled towards regenerated LFP with tailored Li–Fe anti-sites content and recovered surface. Assisted by N-atoms introduction and the pyrolysis of the benzene ring, the regenerated carbon layers displayed high conductivity and low roughness. After cycling, the uniform and thin CEI films could be noted for as-optimized samples, bringing about considerable cycling stability. As cathodes, their capacity could be maintained at about 134 mAh g^{-1} at 1.0C after 500 cycles. After 1000 loops, their capacity retention ratio could be kept at about 92.2% at 5.0 °C. More significantly, the relative regeneration and failure mechanism were clearly proposed. The detailed discussions were carried out as follows.

Results and discussion

Herein, through the control of structural traits about reducing agents, the molecular-level structural features of –OH could be successfully tailored, bringing about an interesting regeneration effect in Fig. 1a. Through optimizing their reaction microenvironment, their failed crystalline phase could be recovered with suitable Li–Fe anti-sites, accompanied by the high-conductive carbon coating. Meanwhile, the suitable reduction potential and apparent acidity inhibit the dissolution of Fe-elements at the surface/near-surface, without the formation of by-product Li_3PO_4. Differing from previous reports about repairing manners, the upcycling of surface structure with bulk phase was tailored at the same time. Thus, supported by the formed surface double carbon layers and tailored Li–Fe anti-sites content, the as-regenerated samples displayed considerable electrochemical properties, which are expected to be applied in the high-end market. The relative physical–chemical properties were shown in Fig. 1 and S1–S7. Firstly, for exploring their regeneration effect, high-resolution Fe 2p XPS spectra are displayed in Fig. 1b. Additionally, it can be found that three couples of peaks could be noted about S-LFP, where those at 710.4 eV/723.2 eV, 712.8 eV/725.9 eV, 717.3 eV/730.3 eV are related to Fe^{2+}, Fe^{3+}, and Fe^{2+} with $3d^6$ electron configuration. The existence of Fe^{3+} mainly comes from the loss of active Li-atoms. Interestingly, no peaks about Fe^{3+} could be noted for as-regenerated samples, illustrating that the introduction of reducing agents would enable the successful recovery of the failed crystalline phase. Moreover, about their crystalline structure, the peaks about 17.1°, 20.8°, 25.5°, 35.5°, 42.2°, and 52.6° would be noted for S-LFP and as-regenerated samples in Fig. 1c, indexing to (020), (011), (111), (131), (112) and (042) planes of $LiFePO_4$ (PDF#98-0443). The peaks at 17.1°, 20.8°, and 25.5° correspond to the typical planes from $FePO_4$ (PDF#84-0876), where no peaks about $FePO_4$ could be disclosed for LA-LFP, PA-LFP, and SA-LFP samples, further confirming the transformation of Fe^{3+} to Fe^{2+}. Interestingly, the typical peaks about Li_3PO_4 (PDF#71-1528) could be noted for PA-LFP and SA-LFP in Fig. 1d. As shown in Fig. 1f, the yellow color of the liquid supernatant after solvothermal reactions indicated the presence of Fe elements, which was further confirmed by ICP-MS analysis. Moreover, compared to PA-LFP and SA-LFP, the solution of LA-LFP was not clear, along with the production of black materials. According to previous reports, they may come from the hydrolysis of organic carbon. As is known, with the assistance of high energy, about tyrosine, the phenolic hydroxyl group and benzene ring are prone to be oxidized and polymerized.[23] This leads to the formation of colored molecular products with extended conjugated structures. That is to say, its surface coating may be achieved, differing from PA-LFP and SA-LFP. About the ICP-MS results in Fig. 1e and S3, the value of Li/Fe molar ratios was about 1.08 for LA-LFP, 1.14 for PA-LFP, 1.22 for SA-LFP, much higher than that of S-LFP (0.82), revealing the recovery of crystalline phase. More interestingly, for SA-LFP, it could be noted that the simultaneous increase in Li/Fe ratio and Fe-dissolution, that is to say, the series of Fe-elements could be disclosed. In Fig. S1, it could be noted that their carbon content was in the order of 4.8% about LA-LFP, <4.9% about PA-LFP, and <5.68% about SA-LFP. Meanwhile, the pH value of the reaction solution was in sequence of 7.65 about LA-LFP > 7.45 about PA-LFP > 7.23 about SA-LFP in Fig. S2. Based on the results above, the use of hydroxyproline and serine would bring the improvements of acidity, resulting in the dissolution of unstable crystalline structure, which perhaps led to the inferior regeneration structure. Certainly, with the replenishments of Li-salts, Li_3PO_4 materials were formed for PA-LFP and SA-LFP. Considering the insulativity and electrochemical inertness of Li_3PO_4, their existence would bring the deterioration of structural traits. About their internal structure, HRTEM images were carried out in Fig. 1g, h and S8–S11. For S-LFP, the garbled distribution regions could be noted, where the lattice distance of 0.221 nm was indexed to (221) planes in Region I, and that of 0.218 nm corresponded to (112) planes in Region III. Meanwhile, the local disordered regions could be found in Region II, which is attributed to the repeated charge/discharge resulting in the local collapse of the long-range ordered crystal phase. More significantly, for LA-LFP, a great crystalline phase could be noted, displaying long-range ordered traits, where the lattice

distance of 0.226 nm was indexed to (041) planes in Region I–III, further revealing the successful regeneration of the failure bulk-phase. Thus, it could be summarized that, with the introduction of reducing agents (tyrosine), the failed bulk phase could be successfully regenerated. However, along with the weakening of steric hindrance (tyrosine > hydroxyproline > serine), the unstable structure at high temperature and pressure would induce the generation of acidic molecules, finally resulting in the formation of Li_3PO_4. Thus, through the control of molecular-level structural features, such as spatial steric hindrance and branch chains, the regeneration of S-LFP could be successfully tailored.

Certainly, the traits of bulk-phase, especially Li–Fe anti-sites, served important roles in their enhancements of energy-storage properties. From the previous reports, the content of Li–Fe anti-sites rendered the tailoring of Li-diffusion behaviors.[10,15,24–26] Thus, their Li–Fe anti-sites were explored as shown in Fig. 2. Notably, XRD Refinement was regarded as an effective investigation manner, and Fig. 2a displayed the relative refinement results, where their contents were in order of 0.6% (LA-LFP) < 1.2% (PA-LFP) < 1.7% (SA-LFP) < 2.0% (S-LFP). Obviously, with the introduction of the amino acid, the released protons rendered the transformation from Fe^{3+} to Fe^{2+}, bringing about the lowering of Li–Fe anti-sites content. That is to say, the reducing ability at solvothermal reaction was in the sequence of tyrosine (LA-LFP) > hydroxyproline (PA-LFP) > serine (SA-LFP). Herein, assisted by the effective reducing properties of tyrosine, the content of Li–Fe anti-sites was reduced from S-LFP (2.0%) to LA-LFP (0.6%), which is beneficial for the improvement of Li-diffusion rate at (010) planes, along with the recovery of electrochemical performances. Further exploring their FTIR spectra in Fig. 2d, the peaks at 970 cm^{-1} were related to the

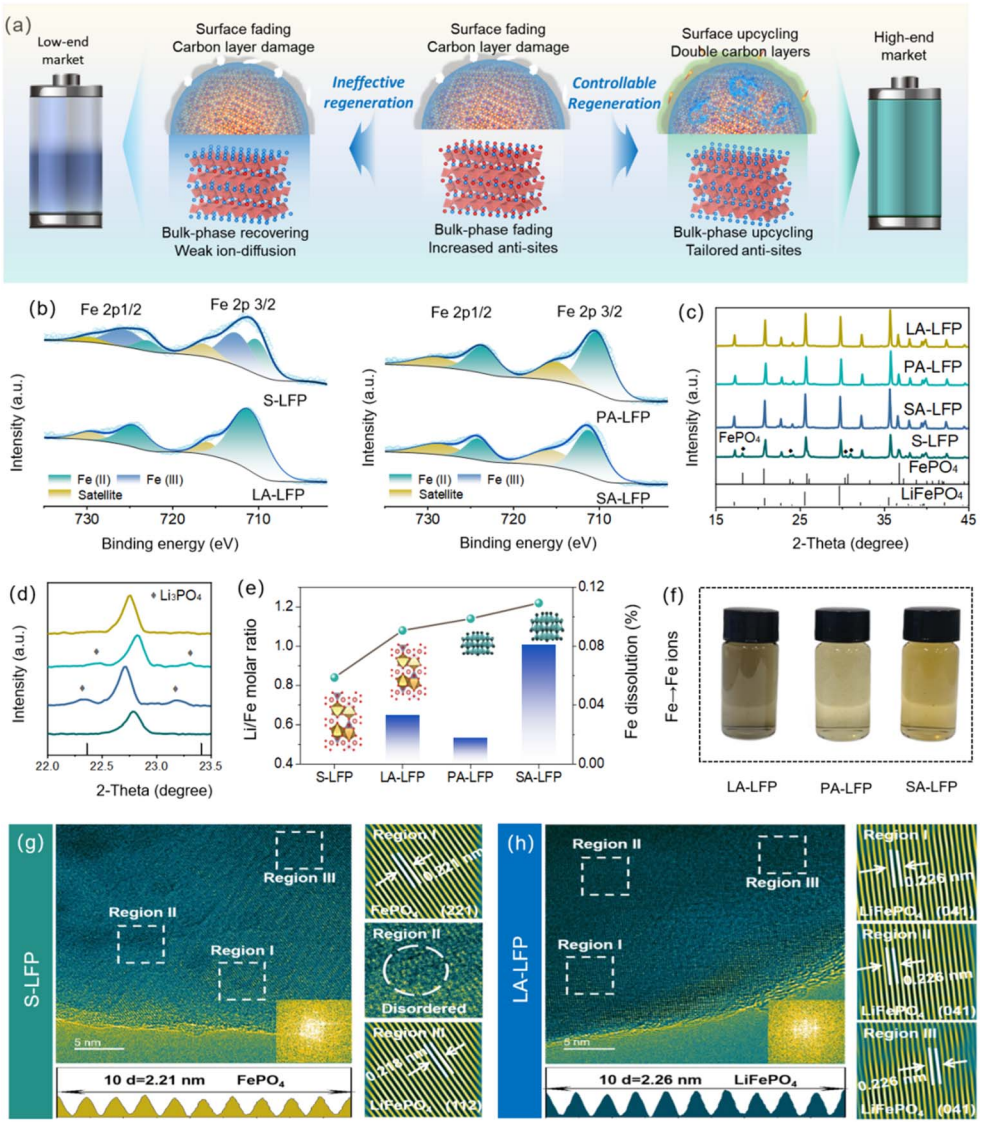

Fig. 1 Schematic illustration of the dual repair of surface structure and bulk phase during the direct regeneration of spent LFP (a), high-resolution XPS of Fe 2p about the as-prepared samples (b), their XRD and local amplifying XRD (c and d), their ICP-MS results (e), the liquid supernatant after solvothermal reaction (f), HRTEM images of S-LFP (g) and LA-LFP (h).

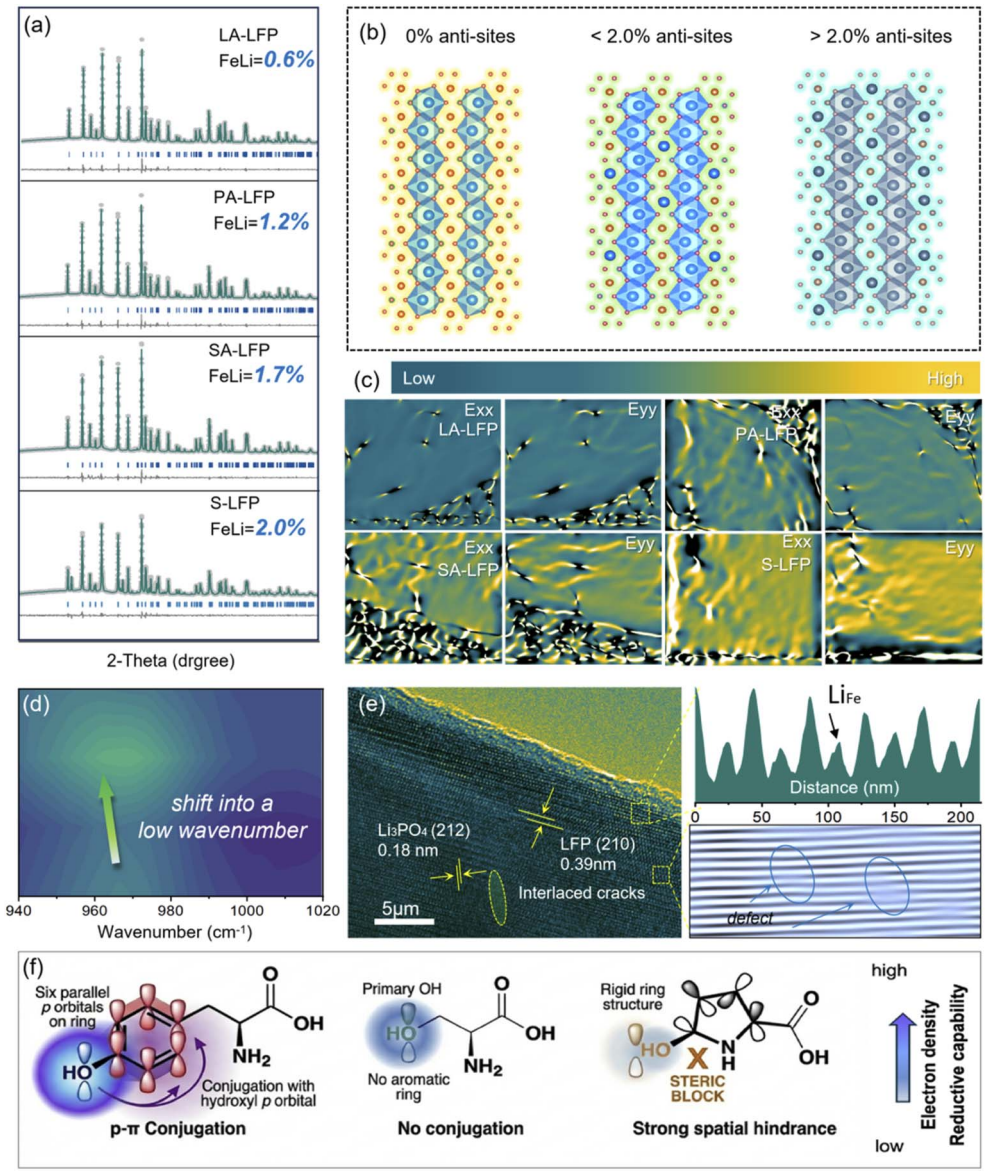

Fig. 2 The exploration of physical–chemical properties in the bulk phase: XRD refinement results (a), the relative Li/Fe anti-sites content (b), their geometric phase analysis (c), counter image of FTIR spectrum (d), HR-TEM images of SA-LFP (e), the reducing mechanism of different chemical structures (f).

$[PO_4]$ tetrahedra, displaying a move toward high wavenumber, which revealed the increase in lithium-iron dislocation defects concentration. Thus, their concentrations were in order of LA-LFP < PA-LFP < SA-LFP < S-LFP. Owing to the different ionic radii of lithium ions (Li^+) and iron ions (Fe^{2+}/Fe^{3+}), this atomic misplacement rendered local lattice distortion and stress concentration in the bulk phase.

Supported by geometric phase analysis (GPA), the visualization analysis of lithium iron dislocation defects was achieved. In Fig. 2c, yellow/black/green regions could be noted, corresponding to tensile strain, compressive strain, and no-strain behaviors, respectively. For S-LFP, it can be observed that the yellow area mostly occupies the stress distribution map. For LA-LFP, the proportion of the green area was increasing, revealing that the lattice compressive strain was alleviated through the repair of inversion defects during amino acid-based reduction repairing, contributing to the improvement of structural stability. Moreover, in Fig. 2e for SA-LFP, the interlayer distance was measured at about 0.18 nm and 0.39 nm, corresponding to the (212) planes of Li_3PO_4 and (210) of LFP, where the interlaced and Li–Fe defects could still be noted, revealing the inferior repairing effect. Thus, it could be deduced that with the *in situ* introduction of f Li_3PO_4 impurity phase, their structural stress would be further improved, perhaps bringing about the inferior electrochemical properties. In Fig. 2f, the reducing mechanism of different chemical structures was explored in detail. Obviously, this sequence is primarily determined by the electron-donating ability of their functional groups and their spatial configuration. For tyrosine, compared to other samples, the strongest reducing ability was exhibited, due to its phenolic

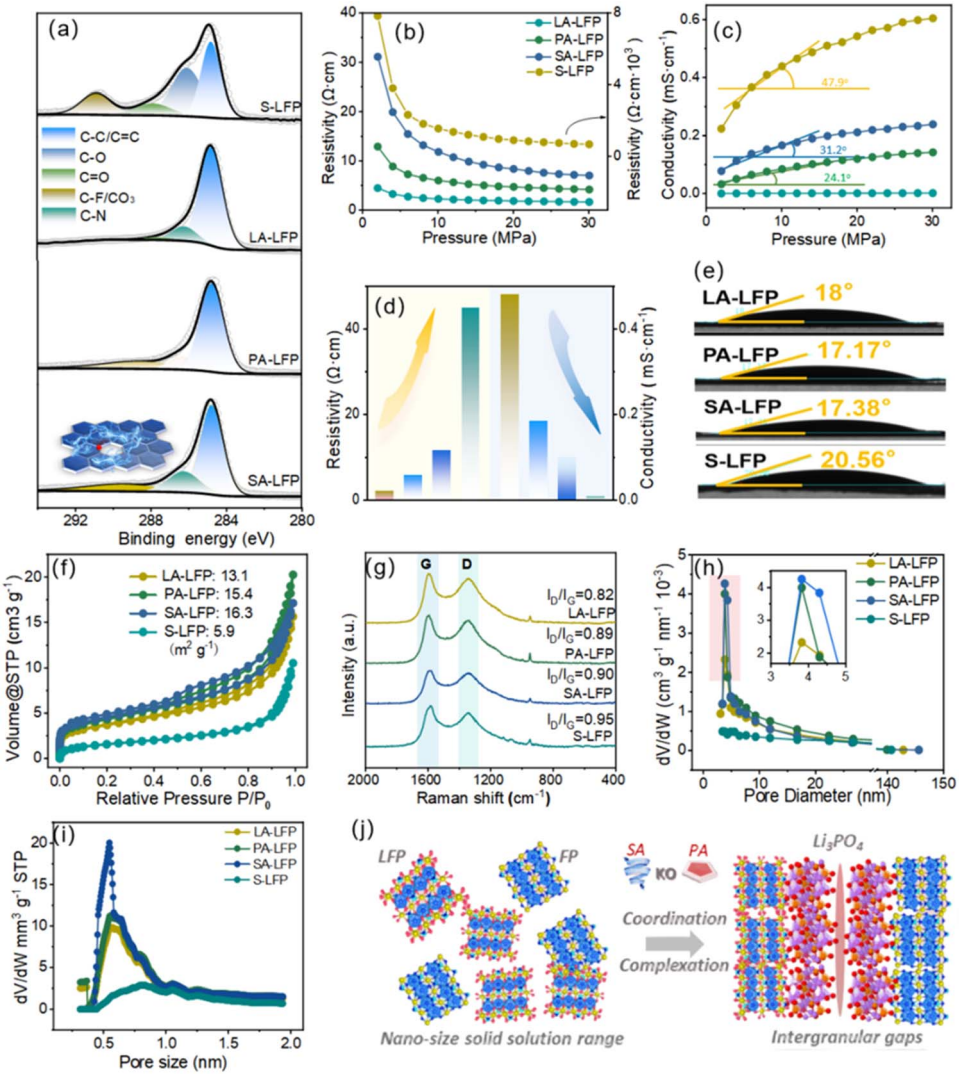

Fig. 3 High-resolution XPS of C 1s about the as-prepared samples (a), the results of resistivity and conductivity (b–d), their contacting angle (e), Raman spectra (g), BET results and pore distribution (f and h), HK plots (i), the formation of nano-cracks (j).

hydroxyl group (–OH). It could be noted that O-atoms of –OH with the benzene ring could be used to form a p-π conjugated system, contributing to increasing electron density and delocalization, enabling efficient electron transferring. For serine, the flexible aliphatic primary hydroxyl group (–CH_2OH) could be noted, showing moderate reducing abilities. Moreover, benefitting from small molecular size and low steric hindrance, the relative reactions could be easily triggered. In contrast, for hydroxyproline, the inferior reducing effect could be detected, where the secondary hydroxyl group (–CHOH–) is attached to the rigid pyrrolidine ring. This cyclic structure displayed considerable steric hindrance, inhibiting the effective contacting with Fe-ions, thus leading to the low electron-donating capacity of –OH. That is to say, in the reduction process, their relative reactivity was determined by the synergistic effects of electronic properties and molecular steric hindrance, which dictate, thus bringing about the evolution of regeneration properties.

With the control of reducing agents, their bulk-phase and surface traits could be effectively tailored. Firstly, their high-resolution XPS C 1s spectra were displayed in Fig. 3a. After fitting peaks, it could be noted that the peaks located at ~284.9 eV, 286.1 eV, 287.9 eV, 290.8 eV were indexed to C–C, C–O, C=O, C–F/CO_3 bonds. The C–F bonds mainly came from the residual PVDF. Interestingly, about the as-regenerated samples, the peak at 286.8 eV could be noted, corresponding to C–N bonds. Obviously, the introduction of an amino acid could induce the doping behaviors of N-atoms. Based on the previous reports, N-doping could be beneficial for accelerating Li^+/e^- moving, bringing about the improved rate properties.[27,28] In Fig. 3b–d, compared to S-LFP, their resistivity was obviously reduced, and their value were in order of LA-LFP < PA-LFP < SA-LFP. Meanwhile, their conductivities were in the sequence of LA-LFP > PA-LFP > SA-LFP. The resistivity and conductivity were related to the traits of the bulk-phase and surface coating layers. Obviously, after regeneration, their failure structure issues were

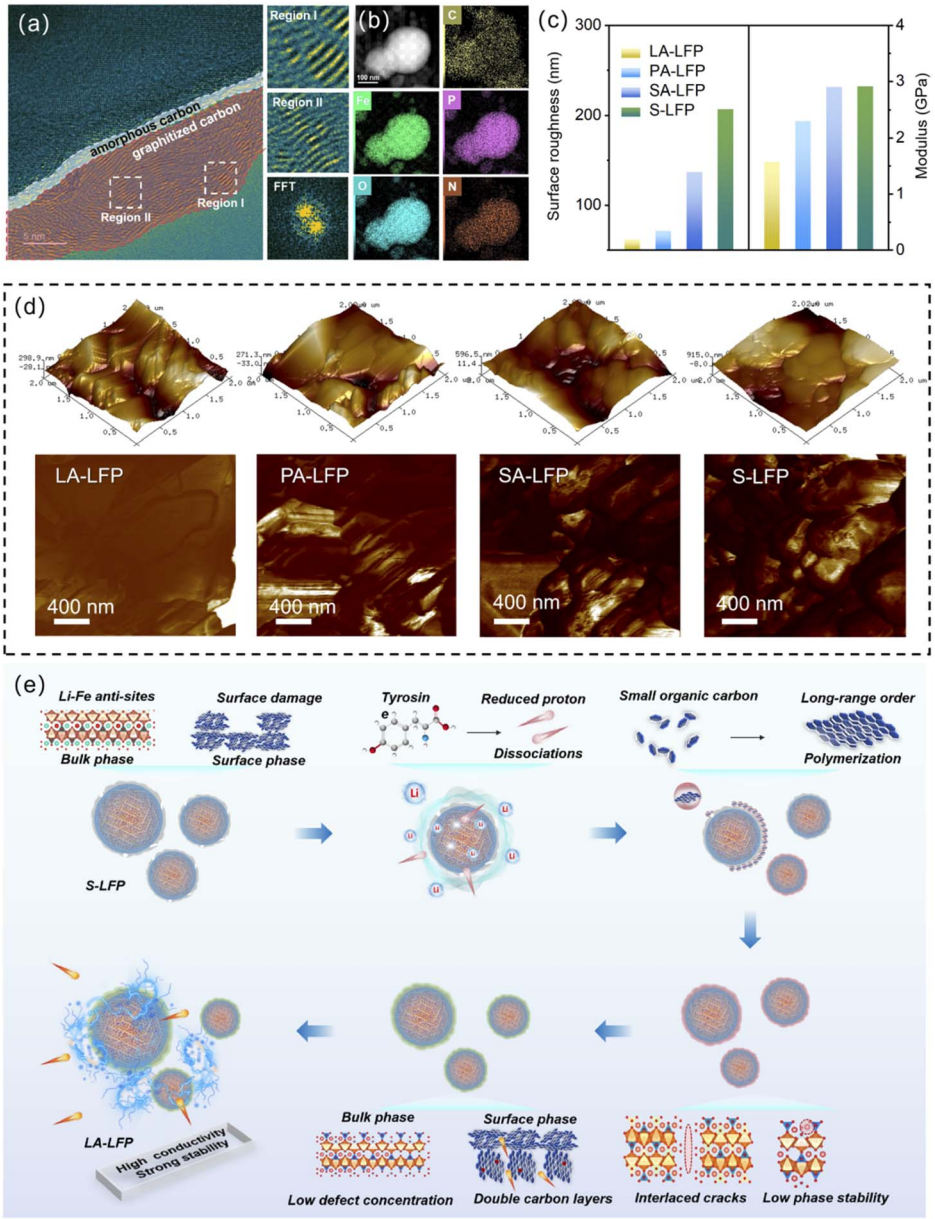

Fig. 4 HR-TEM images and mapping images of LA-LFP (a and b), their surface roughness and modulus (c), their AFM images (d), and the regeneration mechanism (e).

successfully solved. Interestingly, the inflection point slopes of conductivity were about LA-LFP > PA-LFP > SA-LFP, indicating their great interfacial contacting degree and diffusion properties in the bulk phase. With the increase in pressure, the increase in conductivity of LA-LFP was obvious, mainly derived from their great carbon layers. That is to say, the high pressure could induce the contacting of particles, further forming the conductive framework. About their interfacial contacting angles, that of S-LFP could reach up to 20.56°, due to the existence of residual PVDF.

Meanwhile, after regeneration, their contact angles were obviously reduced, illustrating the effective carbonization of surface coating layers. Interestingly, compared to PA-LFP and SA-LFP, LA-LFP shows a contact angle of ~18°, slightly lower than that of S-LFP (~20.56°). This does not indicate inferior hydrophobicity, but rather reflects the removal of residual PVDF (which contributed to the higher contact angle of S-LFP) and the formation of a uniform N-doped carbon layer containing residual functional groups. Obviously, with the increase in the degree of graphitization, the hydrophobicity would also be improved. The LA-LFP surface showed a high graphitization degree, mainly because the benzene ring of tyrosine could be continuously polymerized, further forming a polymer coating layer. Obviously, through the control of branched chain about –OH, the traits of coating layers could also be tailored. Thus, for exploring their practical traits of carbon layers, Raman spectra were carried out as displayed in Fig. 3g, where the peaks at ~1300 cm^{-1} and ~1600 cm^{-1} were associated with D-peaks and

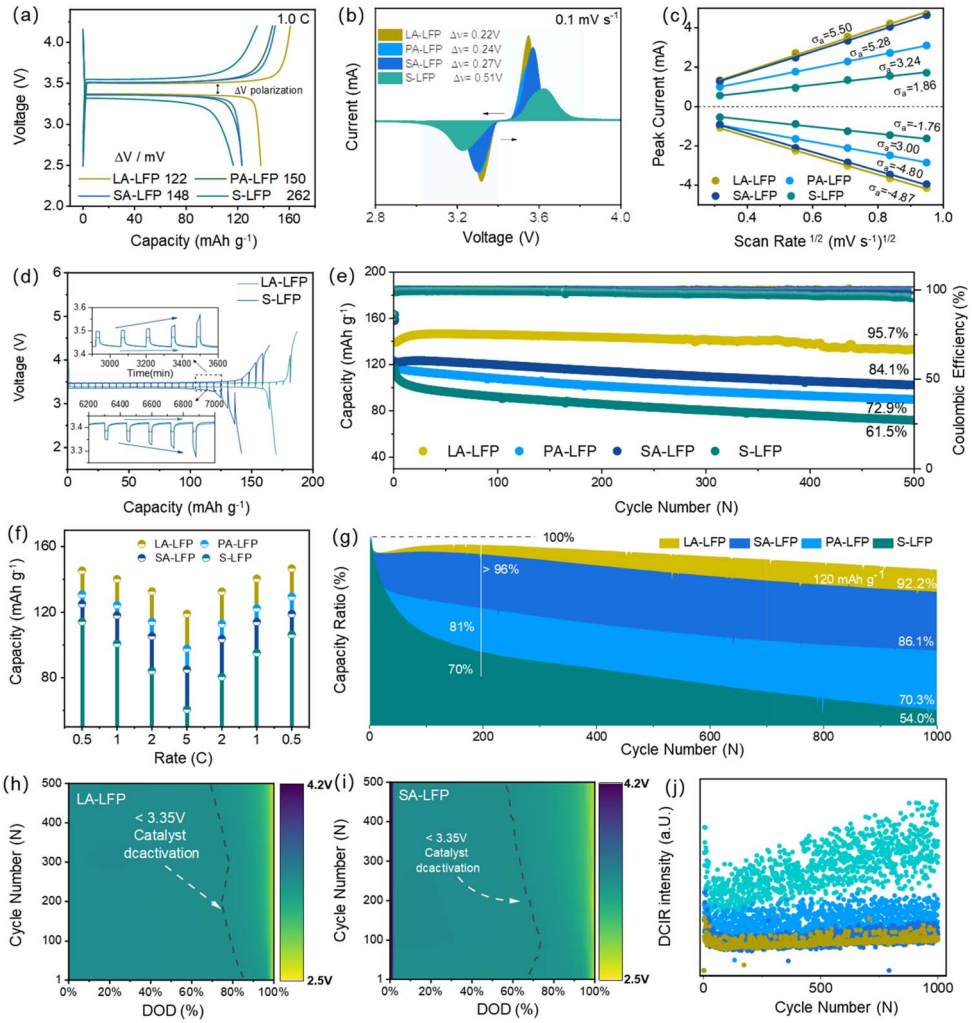

Fig. 5 The exploring of electrochemical properties: charge/discharge platforms (a), CV curves at 0.1 mV s^{-1} (b), the relationship between peak current and scan rate square root (c), GITT curves (d), cycling stability at 1.0C (e) and at 5.0C (g), rate properties (f), contour images of discharge capacity for LA-LFP (h) and SA-LFP (i), DCIR (j) at 1.0C.

G-peaks, corresponding to amorphous carbon and graphitic carbon. Through the evaluation of I_D/I_G, the graphitization degree could be further revealed. Additionally, that of LA-LFP would be up to 0.82, lower than that of other samples, disclosing their great coating layers. In addition, the specific surface area and pore volume distributions were shown in Fig. 3f and h.

Owing to the use of nitrogen absorption and desorption, the residual PVDF induced the blocking of pores, resulting in the relatively small BET result. Additionally, their specific surface areas were in order of 13.1 m^2 g^{-1} (LA-LFP) < 15.4 m^2 g^{-1} (PA-LFP) < 16.3 m^2 g^{-1} (SA-LFP), displaying the high compactness and integrality of LA-LFP. Clearly, with the increase in branched chains, their polymerization would be gradually improved. Through the comparison of pore distribution, the pore volume of LA-LFP was reduced, revealing its upcycling of carbon layers. Interestingly, further exploring the pore distribution at 2.0 nm below, the pore volume could be noted in the sequence of SA-LFP > PA-LFP > LA-LFP. From the previous reports, the pores <2 nm of LFP are mainly derived from nano-cracks, bringing about the inferior energy-storage properties.[29–31] Combining with ICP-MS results, it could be deduced that the strong dissolution ability of Fe-ions about serine rendered the Fe-losing at active regions, that is to say, solid-solution $LiFePO_4$/$FePO_4$, further leading to the formation of nano-cracks as displayed in Fig. 3j. Thus, it could be summarized that, with the effective controlling of –OH branched chain traits, their side reaction could be successfully inhibited.

The surface properties were further explored, as shown in Fig. 4. Firstly, for the LA-LFP surface, two carbon coating layers could be noted. Additionally, contacting LFP directly with pristine carbon layers. After regeneration, the carbon layer successfully recovers. More importantly, LA-LFP can observe a secondary carbon coating layer, which is thicker than PA-LFP and SA-LFP. Different from the original carbon layer, the degree of graphitization can be noticed. In Regions I and II, long-range ordered graphite layers were disclosed, contributing to the enhancements of Li-ion diffusion abilities. Based on the clear

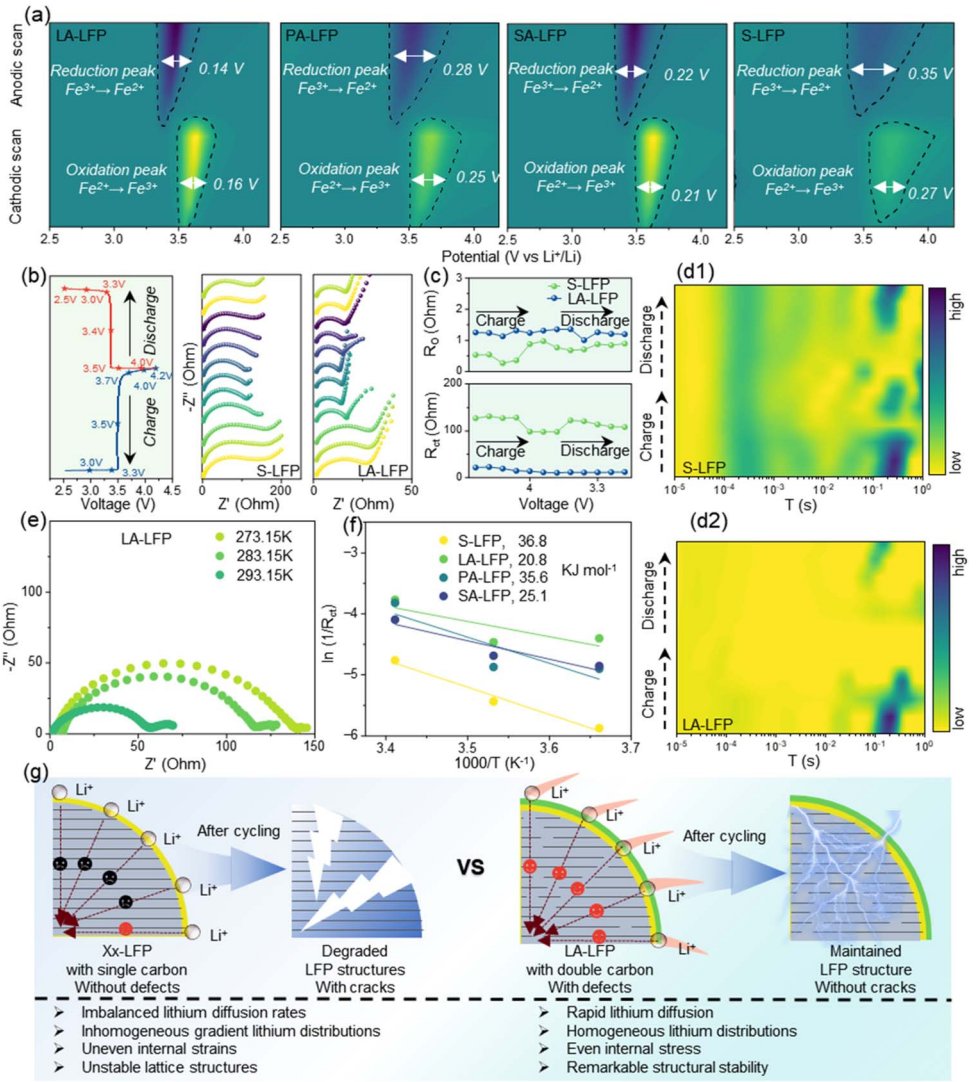

Fig. 6 The exploring of kinetic behaviors: CV counter images (a), Nyquist lots at different voltages (b) and the relative resistance value (c), the transforming of τ during charge/discharge about S-LFP (d1) and LA-LFP (d2), their Nyquist plots at different temperatures (e) and Arrhenius plots for activation energy (f), the advantages of LA-LFP over other LFPs (g).

dots in SAED, the carbon layers with a high degree of crystallinity were further revealed. Obviously, supported by the optimization of branched chains, their surface traits could be effectively tailored. In Fig. 4b, the uniform element distribution could be found, indicating the effective regeneration of S-LFP. More significantly, N-element images could be noted for LA-LFP, revealing the introduction of N-element. From the previous, the *in situ* introduced non-uniform interfaces could be used to enhance the d-band center of iron atoms, bringing about the effective cycling stability. In Fig. 4c, the surface roughness and modulus were displayed. It could be noted that the value of surface roughness of as-regenerated samples was larger than that of S-LFP. From the previous reports, after cycling, the surface could be seriously deteriorated.[12] Moreover, with the increase in surface roughness and modulus and branch molecular weight, the value was in order of LA-LFP < PA-LFP < SA-LFP, revealing the better recovery of surface traits. As is known, the smooth surface contributed to the uniform CEI films forming, resulting in the relatively stable cycling properties. Interestingly, compared to PA-LFP, that of SA-LFP displayed an obviously increased value, mainly derived from the formation of by-product Li_3PO_4 and defects on the sub-surface. Through the analysis of modulus comparison, the relatively small value of LA-LFP could be noted; meanwhile, the large value could be disclosed for other samples. Among them, for PA-LFP and SA-LFP, they mainly derived from partially repaired carbon layers and Li_3PO_4 forming. For S-LFP, they originate from the failure surface and defects on the sub-surface. Fig. 4d shows their AFM images, where a smooth surface can be seen for LA-LFP. Some raised materials can be seen for PA-LFP and SA-LFP, indicating their non-uniform surfaces. Based on the discussion above, the relative repairing mechanism was proposed in Fig. 4e. Based on the previous reports, about S-LFP, the degradation of electrochemical properties mainly comes

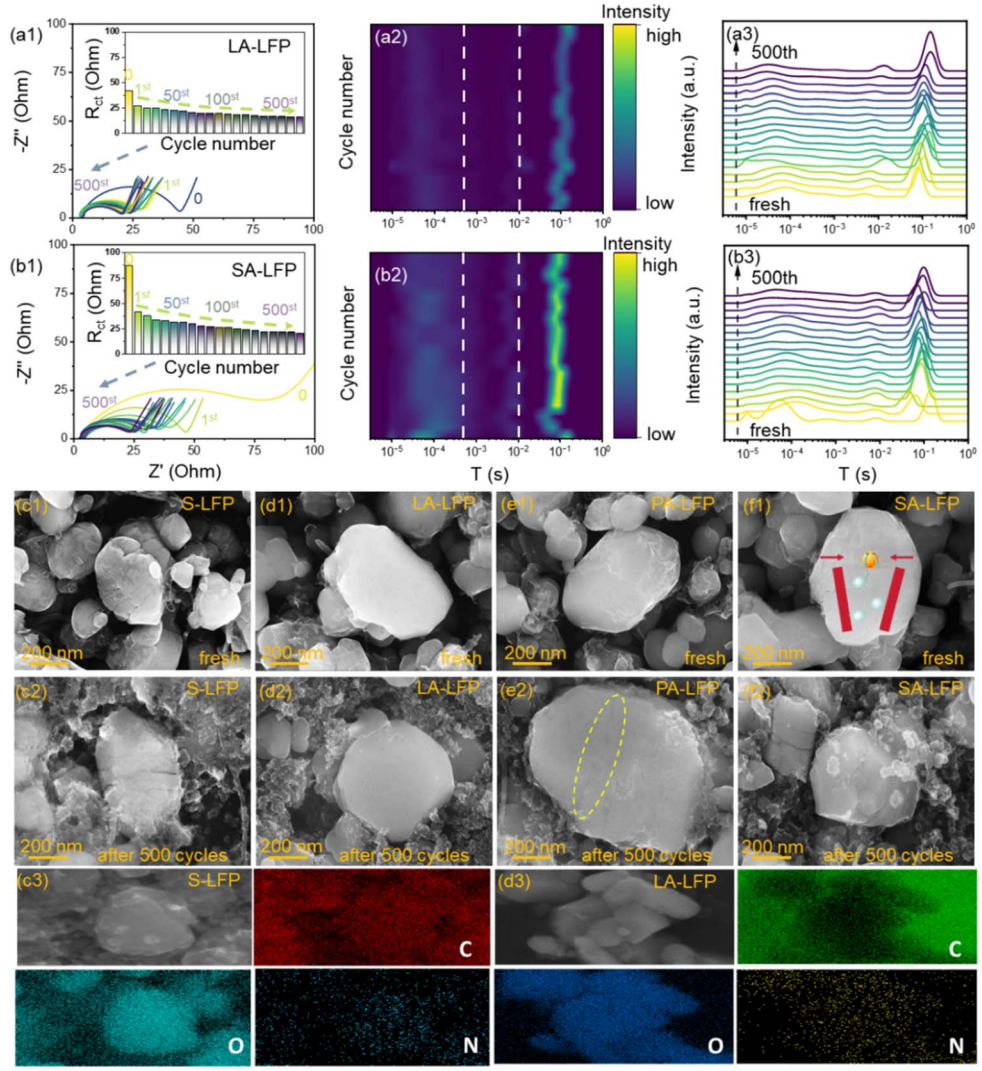

Fig. 7 The exploration of physical–chemical evolution during cycling: Nyquist plots at different cycles, the transformation of τ from pristine to 500th about LA-LFP (a1–a3) and SA-LFP (b1–b3), SEM images and mapping images before/after cycling about S-LFP (c1–c3), LA-LFP (d1–d3), PA-LFP (e1–e2), SA-LFP (f1–f2).

from two issues: (1) bulk-phase fading, including the increase in Li–Fe anti-sites and the dissolution of Li-elements, (2) surface-phase fading, containing the destruction of surface carbon layers, such as rough surface with uneven CEI films formation.[10] That is to say, the traditional repairing manners always focus on solving single failure issues, hardly bringing about the effective recovery of energy-storage properties. Thus, with the introduction of tyrosine, they could serve as bifunctional reagents, reducing agents, and replenishing carbon resources. Firstly, through electron delocalization, its phenolic hydroxyl group could be used to form a stable phenoxy radical during oxidation, displaying strong reducing properties. Thus, the transformation from Fe^{3+} to Fe^{2+} was triggered. Meanwhile, the adequate Li resources enabled the regeneration of $LiFePO_4$ through the reaction between $FePO_4$ and Li elements, finally leading to the pre-repairing of the bulk phase. That is to say, with the lack of sufficient temperatures, their crystalline degree was relatively low, with unstable crystalline phase architecture. Meanwhile, with the further improvement in reaction temperature, the small organic materials would be absorbed on the surface of S-LFP through the hydrogen bonds and electrostatic interactions of the amino group ($-NH_2$) and carboxyl group (–COOH). Then, the organic layers could be formed on the surface. With the support of high temperature, the natural aromatic hexacyclic rings could be kept, inducing the reaction of crosslinking and condensation polymerization. Additionally, they could not only be used to repair the damaged carbon layer, but also form high-conductive carbon layers. At the same time, the stability of the bulk phase and the changing of Li-ions and Fe-ions at incorrect positions could be further improved, with considerable structural stability. Also, through the tailoring of Li–Fe anti-sites contents and surface upcycling, the as-regenerated samples could be expected to be applied in the high-end market.

Given their evolution of physical–chemical properties, their electrochemical behaviors were explored in Fig. 5 and S12–S15.

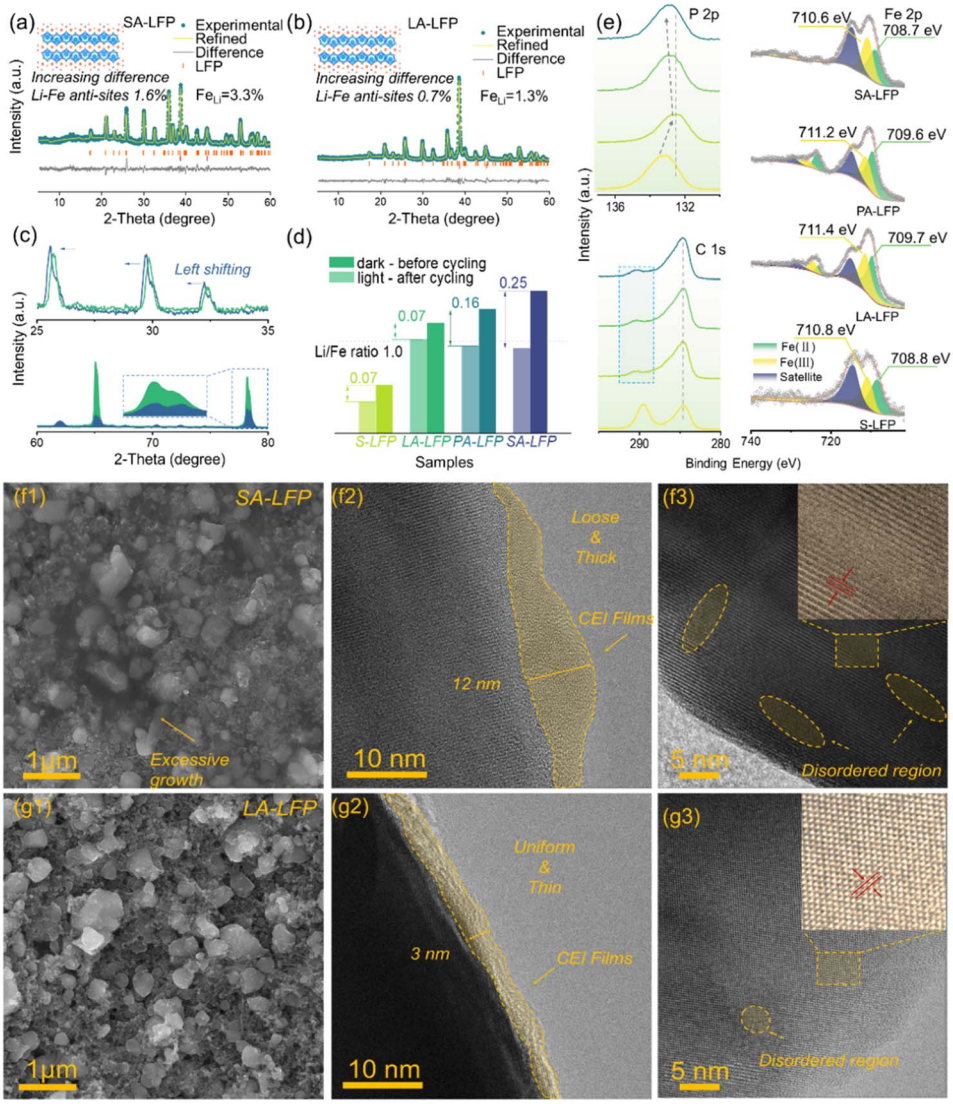

Fig. 8 The *ex situ* exploration of as-regenerated samples after cycles (fully discharged): XRD patterns of SA-LFP and LA-LFP (a–c), ICP results (d), their XPS spectra (e), and SEM and HRTEM images of SA-LFP (f1–f3) and LA-LFP (g1–g3).

Their initial charge/discharge platforms were displayed in Fig. 5a, where their initial capacities were about 139.2 mAh g^{-1} (LA-LFP) > 123.3 mAh g^{-1} (PA-LFP) > 121.7 mAh g^{-1} (SA-LFP) > 118.8 mAh g^{-1} (S-LFP) at 1.0C. Their values of voltage difference (ΔV) were about 122 mV for LA-LFP, 150 mV for PA-LFP, 148 mV for SA-LFP, and 262 mV for S-LFP. Compared to other kinds of –OH, about LA-LFP, the phenolic hydroxyl group ($-C_6H_4-OH$) exhibited stronger reducing abilities, due to the existence of p-π conjugated system. That is to say, the electron cloud of O-atoms from –OH would extend to the entire benzene ring, resulting in the electron cloud density of O–H bonds, further releasing more hydrogen protons with strong reducing ability. Interestingly, compared to the ΔV value of S-LFP, those of regeneration were greatly lowered, revealing successful regeneration. Interestingly, although the capacities of PA-LFP and SA-LFP were similar to that of S-LFP, their ΔV were clearly different from that of S-LFP. Thus, it could be deduced that two reasons: (1) the loss of active material, (2) the existence of Li_3PO_4, and (3) the incomplete surface coating layers. Fig. 5b shows their CV curves at 0.1 mV s^{-1}. About S-LFP, the widening oxidation/reducing peaks could be found, mainly ascribed to the failure of lattice properties, enabling the broadening of reaction energy across different phase regions. Significantly, the relatively narrow peaks could be found for as-regenerated samples, revealing the recovery of the crystalline phase. Among them, that of LA-LFP showed the smallest peak width at half heights, due to the least content of defects and nano-cracks. In addition, it could be noted that their oxidation peaks have a red shift, and their value of peak voltages was in order of LA-LFP < PA-LFP < SA-LFP < S-LFP. Obviously, after regeneration, the Fermi level of LFP about ion-diffusion levels would be lowered, enabling a more easily insertion/de-insertion process. Further exploring their voltage difference, their values were about in the sequence of 0.22 V (LA-LFP) < 0.24 V (PA-LFP) < 0.27 V (SA-LFP) < 0.51 V (S-LFP),

matching well with the results of charge/discharge platforms. Moreover, through linear fitting of peak current and scan rate square root, their value of slope could be noted, where relative values were about 5.50/−4.87 (LA-LFP), 3.24/−3.0 (PA-LFP), 5.28/−4.8 (SA-LFP), and 1.86/−1.76 (S-LFP). Moreover, based on the equation ($i = 0.4463(F^3/RT)^{1/2}n^{3/2}AD^{1/2}CV^{1/2}$), their relative diffusion coefficients were about 2.35×10^{-13}, 0.85×10^{-13}, 2.19×10^{-13} and 0.275×10^{-13} $cm^2\ s^{-1}$, respectively. Obviously, LA-LFP showed the highest diffusion ability. Regarding the PA-LFP samples, a relatively low diffusion coefficient could be found.

Through the comparison of serine and hydroxyproline, the hydroxyl group is located on the pyrrolidine ring, along with the relatively large steric hindrance, inhibiting direct contact with failure materials. Moreover, the weak electronic delocalization may bring about a reduction in the number of electrons released, resulting in inferior reducing ability. Moreover, their residual capacity and capacity retention ratio were about 134 mAh g^{-1} (95.7%, LA-LFP), 89 mAh g^{-1} (72.9%, LA-LFP), 103 mAh g^{-1} (84.4%, LA-LFP), and 71 mAh g^{-1} (61.5%, LA-LFP). Even at 5.0C, their initial capacity was still kept at about 119.8 mAh g^{-1}, 101.99 mAh g^{-1}, 99.66 mAh g^{-1}, and 93.2 mAh g^{-1}, respectively. After 1000 cycles, their capacity retention ratios were about 92.2%, 70.3%, 86.1% and 54.0%. In Fig. 5f, it could be noted that, the capacity of LA-LFP were about 146.7 mAh g^{-1} at 0.5C, 140.5 mAh g^{-1} at 1.0C, 132.6 mAh g^{-1} at 2.0C and 119.8 mAh g^{-1} at 5.0C, much higher than that of other samples PA-LFP (125.2 mAh g^{-1}, 118.2 mAh g^{-1}, 105.5 mAh g^{-1}, 85.1 mAh g^{-1}), SA-LFP (130.9 mAh g^{-1}, 124.5 mAh g^{-1}, 114.3 mAh g^{-1}, 97.9 mAh g^{-1}) and S-LFP (114.3 mAh g^{-1}, 100.9 mAh g^{-1}, 84.3 mAh g^{-1}, 60.7 mAh g^{-1}). The results above confirmed the strong structural stability of LA-LFP. The long-term cycling stability. The battery's performance was further assessed through polarization voltage evolution over 500 cycles at 1C. Here, the yellow region indicates a highly polarized state with a discharge voltage below 3.35 V. Compared to SA-LFP, LA-LFP maintained low polarization throughout the entire 500 cycles. Their charge/discharge median voltages are displayed in Fig. S14. Obviously, S-LFP showed a rapid increase in voltage, along with the large voltage difference. Moreover, compared to other samples, that of LA-LFP was stabilized at ~3.4 V, mainly derived from the stable Li-ions insertion/extraction behaviors. That is to say, benefitting from the strong reducing properties of –OH about LA-LFP, plenty of Fe^{3+}-ions were effectively transformed towards Fe^{2+}, along with the recovery of pristine crystalline phase. Benefiting from the previous reports, the stable median voltage was conducive to the utilization of energy, with small amounts of heat released. Furthermore, Fig. 5j exhibited their DCIR at different cycles. Additionally, their stabling tendency was in order of LA-LFP > SA-LFP > PA-LFP > S-LFP. Owing to the existence of Li_3PO_4 and phase vacancies, the stabilities of PA-LFP and SA-LFP were lowered. Further exploring their internal resistance in Fig. S15, it could be noted that, with increasing cycling, the difference in internal resistance was large, due to their failure structure. Moreover, in comparison with other samples, the internal resistance of LA-LFP was about 45 Ω, revealing its fast ion-diffusion ability.

Thus, it could be summarized that, with optimization of reducing agents, the as-regeneration LA-LFP showed considerable electrochemical properties, mainly ascribed to the successful recovery of bulk-phase and surface coating layers. But, owing to the by-product Li_3PO_4 and phase vacancies formation, the regenerated properties of SA-LFP and PA-LFP hardly meet the demand of energy-storage systems, due to the inferior structural properties with unstable ion-diffusion behaviors.

Capturing their interesting evolution of electrochemical properties, the detailed kinetic behaviors were carried out in Fig. 6 and S16–S19. Firstly, the counter images from CV curves at different scan rates were obtained in Fig. 6a. It could be found that, compared to other samples, the couple peaks of LA-LFP were more symmetrical, revealing their greater reversibility. Meanwhile, the peaks of LA-LFP were sharper than those of other samples, indicating a better linear relationship between peak current and scan rate. That is to say, the optimized LA-LFP displayed stronger rate properties, matching well with the results of the electrochemical properties. Moreover, about the redox peak, the relative value of peak width at half height could be noted in order of LA-LFP (0.14 V, 0.16 V) < SA-LFP (0.22 V, 0.21 V) < PA-LFP (0.28 V, 0.25 V) < S-LFP (0.35 V, 0.27 V). For further exploring the effect of reducing agent (tyrosine) on the evolution of physical–chemical properties about LA-LFP, the *in situ* Nyquist Plots were carried out as displayed in Fig. 6b. Different voltages (2.5 V, 3.0 V, 3.3 V, 3.4 V, 3.5 V, 4.0 V, 4.2 V) were selected, where the semicircle at high frequency was related to charge transferring resistance (R_{ct}), and the oblique line at low frequency was associated with diffusion resistance. It could be noted that, assisted by the introduced tyrosine, the value of R_{ct} about LA-LFP was clearly lowered. From the discussions above, the derived surface carbon layers with a high graphitization degree served important roles for their surface Li^+/e^- diffusion. After fitting, the relative ohmic resistance (R_o) was obtained, which was related to the natural traits of materials. In addition, Fig. 6c revealed the change in R_o and R_{ct} during the charge/discharge process. Regarding S-LFP and LA-LFP, a similar and stable R_o value was disclosed during cycling, illustrating high consistency of battery assembling. In addition, about S-LFP, the R_{ct} value was obviously reduced to 4.0 V and 4.2 V during charging, mainly originating from the formed CEI and the transformed Li-lacking phase from the Li-rich phase. Interestingly, further discharging, that of S-LFP was further increasing, meanwhile that of LA-LFP was slightly reducing, then stabilizing. According to the previous reports, the results above came from the effective carbon layers of LA-LFP, which contributed to the establishment of stable interfacial structures.[26,28] In comparison, the R_{ct} value of S-LFP was unstable, mainly because the carbon layer was deteriorated during cycling, rendering the uneven CEI formation. Assisted by distributing relaxation time (DRT), it could be noted that, τ_1 (ranging from 10^{-5} to 3×10^{-4}) was associated with the contacting resistance between current collectors and active materials. Furthermore, τ_2 (ranging from 10^{-2} to 1) was related to R_{ct}. About τ_1, the low peak value of LA-LFP could be noted, revealing the great conductivity of carbon fibers between particles. That is

to say, for LA-LFP, the considerable carbon layers served important roles in 3D electron transport pathways, boosting the reduction in R_o and contacting resistance. More significantly, about τ_2, the reduced diffusion resistance could be noted for LA-LFP, illustrating the formed uniform CEI with high conductivity, which was derived from the recovering bulk-phase and surface carbon layers. Additionally, τ_3 corresponded to the electrochemical activities of R_{ct} in the bulk phase; meanwhile, the small value revealed the regenerated samples with low defect-concentration and high-ordered olivine crystal phase, which could provide stable paths for Li-moving. In addition, their Nyquist plots at different temperatures were shown in Fig. 6e. With the lowering of temperature, their resistance was further improved, mainly ascribed to the lowering of the Li^+/e^- diffusion coefficient. Additionally, based on Arrhenius equations ($R_c^{-1} = A_o \exp(-E_a R^{-1} T^{-1})$), their diffusion energy barriers were calculated to be in the order of 20.8 kJ mol^{-1} of LA-LFP < 25.1 kJ mol^{-1} of SA-LFP < 35.6 kJ mol^{-1} of PA-LFP < 36.8 kJ mol^{-1} of S-LFP. Obviously, the low diffusion energy barrier was beneficial for the ion moving behaviors. Additionally, the established double high-conductive carbon layers were beneficial for interfacial transferring. Significantly, through the tailoring of Li–Fe anti-sites content and the establishment of carbon layers, the as-optimized samples could display rapid lithium diffusion and even internal stress, along with remarkable structural stability. Thus, it could be summarized that, with the introduction of a highly effective reducing agent (tyrosine), the recovery of crystalline phase and surface coating layers could be successfully achieved, with the lowering of internal resistance and the broadening of ion-diffusion paths.

Meanwhile, the evolution of as-regenerated samples was carried out during cycling. The Nyquist plots, DRT analysis, and SEM images are shown in Fig. 7. Firstly, in the pristine state, the R_{ct} value of LA-LFP is smaller than that of SA-LFP, mainly ascribed to the broadened ion-diffusion paths without the formation of Li_3PO_4. Moreover, after the electrochemical activities, an obvious reduction in resistance can be noted, due to the formation of high-conductivity CEI films. Interestingly, the reduction values were about 40 Ω for SA-LFP and 12 Ω for LA-LFP. More CEI films formed on the surface of SA-LFP, along with the serious consumption of the electrolyte. Based on the results above, it could be revealed that too many excess formation CEI films were produced on the surface of SA-LFP, which would lead to inferior electrochemical properties. Additionally, at 1st cycling, the main CEI formation could be formed, mainly including compact LiF layers (internal surface regions) and loose organic layers (outer surface regions). Meanwhile, with cycling, the gradual decrease in R_{ct} could be detected and stabilized, matching well with the results from previous reports.[32,33] As is known, the stable CEI films served important roles in their energy-storage properties, especially cycling stability and interfacial ion-diffusion behaviors. Additionally, after the 500th cycling, the R_{ct} value of SA-LFP remained about ~25 Ω, larger than that of 17 Ω for LA-LFP. Moreover, compared to LA-LFP, the stability of R_{ct} about SA-LFP during cycling was poor, revealing the serious interfacial side reaction and surface behaviors. According to the previous reports, the interfacial and dynamic behaviors could be explored in detail by DRT analysis, further contributing to the evaluation of their surface traits, where the results were displayed in Fig. 7a2, a3 and b2, b3.[34–36] Herein, the short relaxation time (τ_1, ~10^{-5}–3 × 10^{-4} s) was related to the contacting resistance and the electron-moving of different particles, where the peak intensity of LA-LFP was always lower than that of SA-LFP. The results above revealed that the as-derived double carbon layers were beneficial for increasing surface conductivity, bringing about the lowering of contacting resistance between particles and the current collector. Additionally, the typical relaxation time (τ_2, ~10^{-2}–1 s) was associated with the electrochemical transferring process, where the DRT peaks intensity was slowly changing, revealing their rapid and stable intrinsic reaction kinetics. It could be deduced that the high crystalline LA-LFP with fewer defects could offer effective ion-diffusion paths. In addition, after 500 cycles, their morphology structures were exhibited in Fig. 7c–f. It could be noted that, about fresh samples, the surface roughness was in order of LA-LFP < PA-LFP < SA-LFP < S-LFP. Meanwhile, the clear cracks could be noted for S-LFP due to the repeated cycling. Additionally, in the as-regenerated SA-LFP and PA-LFP, the crack could still be noted, although with the coalescence to some extent. Obviously, the formed Li_3PO_4 on the crack regions inhibited the growth of the crystal phase, that is to say, it served as "external substances" to prevent the "wound healing". Meanwhile, through the precise control of the reduction reaction, the smooth surface could be noted for LA-LFP, where the results could coincide well with AFM. Meanwhile, in Fig. 7c3 and d3, about LA-LFP, the relative N-elements distribution could be found, further revealing the introduction of N-elements. Moreover, after cycling, the relatively smooth surface could also be found for LA-LFP. Additionally, compared to their fresh samples, S-LFP, PA-LFP, and SA-LFP displayed more serious grain cracks. Obviously, the pristine cracks would bring about an increase in stress in the bulk phase, further leading to serious structural fading. Thus, it could be summarized that the as-regenerated LA-LFP displayed a smooth surface without the grain cracks, boosting the improvements of internal ion diffusion. Moreover, the establishment of double high-conductive carbon layers was beneficial for reducing interfacial resistances, finally bringing about considerable cycling stability and rate properties.

Fascinated by their evolution of physical–chemical properties, their *ex situ* properties were further explored in Fig. 8. Based on Refined results, the content of Li–Fe anti-sites was about 1.3% of LA-LFP and 3.3% of SA-LFP. Compared to pristine samples, the increasing content was about 0.7% about LA-LFP and 1.6% about SA-LFP in Fig. 8a and b. Based on the previous investigation, when the Li_{Fe} content was lower than 2.0%, the existence of Li–Fe anti-sites was beneficial for the ion-diffusion behaviors. Moreover, in comparison with LA-LFP, the residual crack and relatively many Li–Fe anti-sites would induce a rapid increase in the number of anti-sites. In addition, in Fig. 8c, the left-shifting of XRD peaks could be noted for SA-LFP, revealing the expansion of interlayers along with inferior structural stability, mainly derived from the increased Li–Fe anti-sites content. Moreover, to a high degree, the split peaks

could be noted, with the lowering of peak intensity, illustrating the existence of Li–Fe anti-sites and lattice distortions. Thus, the tailoring of Li–Fe anti-sites content was vital for the as-regenerated samples. Through the comparison of high-resolution spectra, P 2p and C 1s in Fig. 8e, it could be noted that the peaks of P 2p in the as-regenerated samples were located at low binding energy. Moreover, compared to SA-LFP and PA-LFP, LA-LFP displayed a lower binding energy, indicating a relatively great crystalline structure. As is known, after cycling, some Fe^{2+} ions would be transformed into Fe^{3+} ions, which induced the weakening of electron density about P–O bonds, further revealing the considerable stability of LA-LFP. About C 1s spectra, the relatively stable peaks could be noted, and the peaks at ~290 eV were associated with the formed CEI films (O–C=O, C=O). Additionally, the weak peaks could be noted for LA-LFP, revealing less formation of CEI films. Meanwhile, the strong peaks could be noted for SA-LFP, illustrating their serious side reactions. Meanwhile, for Fe 2p, the peaks of LA-LFP were located at high binding energy, confirming the structural stability of LA-LFP.

Further exploring their *ex situ* morphology and internal architecture, it could be noted that some gel-like materials could be noted for SA-LFP, mainly derived from the formation of too much excess CEI films. Moreover, the clear surface of electrodes could be noted for LA-LFP, indicating their great interfacial electrochemical reactions. Moreover, about their HRTEM, the loose and thick CEI films could be disclosed for SA-LFP (12 nm), meanwhile the uniform and thin CEI films were detected for LA-LFP (3 nm), mainly derived from the smooth surface of double carbon layers with high conductivity. Furthermore, it could be found that, after cycling, some disordered regions could result, and more defects were detected for SA-LFP, with inferior lattice stability. The relatively high crystalline degree was revealed for LA-LFP, illustrating its stable lattice properties. Thus, it could be summarized that the recovery of the crystalline phase could be beneficial for the cycling stability; meanwhile, the enhanced surface contributed to the formation of thin and uniform coating layers, inhibiting the side reactions of the electrolyte.

Conclusions

Herein, the failure issues of S-LFP, including bulk-phase fading and surface destroying, were successfully upcycled towards high-conductive fresh LFP. Benefitting from the p-π conjugated effect of the benzene ring, the strong reducing abilities could be noted for the introduced tyrosine, bringing about the effective transformation from Fe^{3+} to Fe^{2+}. Meanwhile, limited by steric hindrance from rigid pyrrolidine ring groups, the inferior reducing properties could result. More significantly, assisted by aromatic nucleus and rich functional groups, tyrosine could be effectively absorbed on the surface of pre-formed LFP, thus serving as carbon replenishing, finally resulting in the formation of a double coating carbon layer. The adsorbed organic matter could serve an important role for secondary reducing gas, bringing about the changeover of Li–Fe anti-sites. It could be noted that, through the control of electronic delocalization, their internal defect could be effectively tailored, meanwhile inhibiting the formation of by-product Li_3PO_4. The optimized LA-LFP displayed high-conductivity crystalline and surface architecture, along with considerable electrochemical properties. As a Li-storage cathode, it could keep 134 mAh g^{-1} at 1.0C after 500 cycles, and with a capacity retention ratio 95.7%. Even at 5.0C, their initial capacity was still kept about ~120 mAh g^{-1} with a capacity retention ratio of 92.2% after 1000 cycles. Certainly, assisted by detailed kinetic analysis and *ex situ* structural testing, the evolution of anti-sites and coating layers could induce the improvements of ion-diffusion behaviors and the reduction of internal resistance. After cycling, benefitting from the decreased structural stress, the relatively stable structure could be maintained for LA-LFP, along with the uniform CEI formation. Thus, the work is anticipated to shed light on the regeneration effect of different molecular groups, whilst offering controllably repairing strategies for S-LFP towards great energy-storage properties.

Experimental section

Preparation of raw materials and chemical agents

S-LFP came from the industry in Zhejiang province, through the effective manual disassembly and liquid phase exfoliation. The selected chemical agents were purchased from Sinopharm Chemical Reagent Co., Ltd, without further purification.

Regeneration of S-LFP

Herein, the typical solvothermal reaction was carried out to induce the transformation of S-LFP to fresh LFP. Firstly, 45 mL of deionized water was added to the polytetrafluoroethylene tank with a 100-mL capacity. Then, after the weighing of 0.045 mol lithium acetate and 0.045 mol reducing agents, they were further introduced into the same polytetrafluoroethylene tanks. In addition, 3 g of S-LFP was subsequently added. After 10 min of ultrasonic processing and 30 min of magnetic stirring, a relatively uniform mixing solution could be obtained. The tanks were further transferred into stainless steel housing and sealed tightly. They were placed in an air blast drying oven with the reaction conditions (180 °C, 6 h). After natural cooling, the reaction products were further washed with the assistance of ethanol and deionized water (3 times). The as-obtained materials were further dried at 80 °C for 6 h. Finally, they were placed in a tubular furnace with the protection of Ar/H_2. The sintering conditions were about heating rate (5 °C min^{-1}), holding temperature (750 °C), and holding time (2 h). The as-prepared samples could be regarded as regenerated LFP, and due to the utilization of different reducing agents (tyrosine, hydroxyproline, and serine), they were named LA-LFP, PA-LFP, and SA-LFP, respectively.

Characterization of as-prepared samples

For exploring their crystal structure, X-ray diffraction (XRD, Rigaku SmartLab) and Raman spectra (Renishaw inVia) were carried out. To explore their surface evolution, Fourier transform infrared spectroscopy (FTIR, Thermo Scientific Nicolet

iS20), atomic force microscope (AFM, Bruker Dimension Icon), contact angle meter (Krüss DSA25), and X-ray photoelectron spectroscopy (XPS, Thermo Scientific Escalab 250Xi) were applied. Also, the content of metal-based elements was explored by inductively coupled plasma mass spectrometry (ICP-MS, Agilent 7900). Meanwhile, their resistivity and specific surface area were investigated by Four-Point Probes (ST2742B, Four Point Probes & Keithley) and Brunauer–Emmett–Teller (BET, Micromeritics TriStar II Plus). Certainly, the morphology and internal traits were explored by scanning electron microscope (SEM, JSM-7600F, JEOL) and transmission electron microscope (TEM, JEOL JEM-F200).

Preparing cell devices

The relative cell process is described in detail in our previous report.[37] Herein, the content of active materials was about $\sim$3.0 mg cm^{-2}. The electrochemical testing conditions were also similar to those in our previous work.

Author contributions

Y. C. and X. C. contributed equally to this work. Y. C. and X. C. contributed to investigation, validation, literature collection, writing of original draft, editing of revised manuscript. Z. Z. contributed to data curation and response to reviewer. W. S., and Y. Y. contributed to review and editing. P. G. contributed to conceptualization, supervision, and writing – review and editing. All authors discussed the results and commented on the manuscript.

Conflicts of interest

There are no conflicts to declare.

Data availability

The data supporting this article have been included as part of the supplementary information (SI). Supplementary information: detailed structural and electrochemical characterization of regenerated $LiFePO_4$ materials. The figures (Fig. S1–S21) display carbon content, pH values, particle size distribution, XPS, FTIR, TEM, and various electrochemical tests including charge–discharge profiles, cyclic voltammetry, diffusion coefficients, and impedance spectroscopy at different temperatures. The tables (Tables S1–S6) summarize Rietveld refinement results from XRD, providing lattice parameters, phase ratios, and Li–Fe anti-site defects. Together, these data systematically support the effectiveness of the amino acid-assisted regeneration strategy. See DOI: https://doi.org/10.1039/d6sc01492e.

Acknowledgements

This work was financially supported by the National Natural Science Key Foundation of China (52534010) and National College Students Innovation and Entrepreneurship Training Program (202510533021).

References

1 X. X. Wu, Y. H. Liu, J. X. Wang, Y. H. Tan, Z. Liang and G. M. Zhou, *Adv. Mater.*, 2024, **36**, 2403818.
2 T. Yang, D. Luo, A. Yu and Z. Chen, *Adv. Mater.*, 2023, **35**, 2203218.
3 M. T. Zheng, Y. You and J. Lu, *Nat. Rev. Mater.*, 2025, **10**, 355–368.
4 J. X. Wang, J. Ma, Z. F. Zhuang, Z. Liang, K. Jia, G. J. Ji, G. M. Zhou and H. M. Cheng, *Chem. Rev.*, 2024, **124**, 2839–2887.
5 H. C. Ji, J. X. Wang, J. Ma, H. M. Cheng and G. M. Zhou, *Chem. Soc. Rev.*, 2023, **52**, 8194–8244.
6 X. X. Wu, J. Ma, J. X. Wang, X. Zhang, G. M. Zhou and Z. Liang, *Glob. Chall.*, 2022, **6**, 2200067.
7 Z. Zeng, H. Lei, X. Lu, C. Zhu, Y. Wen, J. Zhu, X. Ji, W. Sun, Y. Yang and P. Ge, *Energy Storage Mater.*, 2025, **74**, 103947.
8 Z. H. Zeng, Y. Chen, C. Zhu, H. Lei, W. Sun, Y. Yang and P. Ge, *J. Energy Chem.*, 2026, **112**, 553–571.
9 P. P. Xu, D. H. S. Tan, B. L. Jiao, H. P. Gao, X. L. Yu and Z. Chen, *Adv. Funct. Mater.*, 2023, **33**, 2213168.
10 P. P. Xu, Q. Dai, H. P. Gao, H. D. Liu, M. H. Zhang, M. Q. Li, Y. Chen, K. An, Y. S. Meng, P. Liu, Y. R. Li, J. S. Spangenberger, L. Gaines, J. Lu and Z. Chen, *Joule*, 2020, **4**, 2609–2626.
11 B. Markey, M. H. Zhang, I. Robb, P. P. Xu, H. P. Gao, D. W. Zhang, J. Holoubek, D. Xia, Y. F. Zhao, J. C. Guo, M. Cai, Y. S. Meng and Z. Chen, *J. Electrochem. Soc.*, 2020, **167**, 160511.
12 K. Jia, J. Ma, J. X. Wang, Z. Liang, G. J. Ji, Z. H. Piao, R. H. Gao, Y. F. Zhu, Z. F. Zhuang, G. M. Zhou and H. M. Cheng, *Adv. Mater.*, 2023, **35**, 2370034.
13 P. Wang, J. Zhou, J. W. Huang, P. Yang, Y. C. Zhang, Z. L. Yang, G. R. Wang, D. Guo, J. P. Song and L. F. Fei, *ACS Sustain. Chem. Eng.*, 2025, **13**, 12647–12657.
14 Z. Y. Lai, J. Long, Y. Lu, F. Q. Luo, L. X. Zeng, W. B. Lai, Y. X. Li, Q. R. Qian, Q. H. Chen, K. Zhang, Z. H. Yan and J. Chen, *Adv. Energy Mater.*, 2025, **15**, 2501009.
15 F. F. Li, Z. Zheng and L. Li, *Mater. Lett.*, 2025, **396**, 138792.
16 Y. H. Liao, Z. K. Chai, S. Y. Zhang, Y. M. Zhang, L. Wang, X. J. Qiu, Q. Han, L. L. Xie, L. M. Zhu and X. Y. Cao, *Mater. Today Chem.*, 2025, **49**, 103075.
17 S. Hao, Y. Lv, Y. Zhang, S. Liu, Z. Tan, W. Liu, Y. Xia, W. Yin, Y. Liao, H. Ji, Y. Kong, Y. Shao, Y. Huang and L. Yuan, *Energy Environ. Sci.*, 2025, **18**, 3750–3760.
18 J. Tang, B. Huang, X. Xiao, H. Qu, Y. Song, J. Li, Y. Song, H. Ji, J. Wang, Y. Zhu and G. Zhou, *J. Am. Chem. Soc.*, 2025, **147**, 24594–24603.
19 J. Yang, K. Zhou, R. Gong, Q. Meng, Y. Zhang and P. Dong, *J. Environ. Manage.*, 2023, **348**, 119384.
20 J. Tang, H. Qu, C. Sun, X. Xiao, H. Ji, J. Wang, J. Li, G. Ji, X. Zhang, H. M. Cheng and G. Zhou, *Adv. Mater.*, 2025, **37**, 2420238.
21 D. Tang, G. Ji, J. Wang, Z. Liang, W. Chen, H. Ji, J. Ma, S. Liu, Z. Zhuang and G. Zhou, *Adv. Mater.*, 2023, **36**, 2309722.

22 Z. Zeng, P. Xu, J. Li, C. Yi, W. Zhao, W. Sun, X. Ji, Y. Yang and P. Ge, *Adv. Funct. Mater.*, 2023, **34**, 2308671.
23 C. Lu, Y. Cao, J. Li, X. Wang, H. Xu, Z. Wang, Q. Wan, X. Wei, G. Zhou and Y. Song, *Angew. Chem., Int. Ed.*, 2025, **138**, e18557.
24 Z. Y. Jiang, Z. H. Xu, L. Li, J. W. Wei, Q. H. Liu, Y. C. Chen, T. Xiao, J. Lei and Y. Zhou, *ACS Appl. Mater. Interfaces*, 2025, **17**, 4875–4883.
25 X. Lin, S. Zhang, M. Yang, B. Xiao, Y. Zhao, J. Luo, J. Fu, C. Wang, X. Li, W. Li, F. Yang, H. Duan, J. Liang, B. Fu, H. Abdolvand, J. Guo, G. King and X. Sun, *Nat. Mater.*, 2025, **24**, 83–91.
26 Y. Wu, S. J. Mao, S. R. Xu, Q. Yuan, T. Y. Xiao, Y. Y. Li, Z. Wang, Q. X. Sui, B. Yuan, H. Wen and J. Liu, *J. Environ. Chem. Eng.*, 2025, **13**, 115057.
27 X. Xu, R. Zhao, W. Ai, B. Chen, H. Du, L. Wu, H. Zhang, W. Huang and T. Yu, *Adv. Mater.*, 2018, **30**, 1800658.
28 Y. F. Li, H. X. Yu, Y. Ding, M. T. Huang, Y. H. Xie, P. L. Li, Z. H. Wang, L. H. Wang, L. Chen, X. B. Luo and L. M. Yang, *Chem. Eng. J.*, 2025, **522**, 168096.
29 W. C. Chien, Y. R. Li, S. H. Wu, Y. S. Wu, Z. H. Wu, Y. J. J. Li and C. C. Yang, *Adv. Powder Technol.*, 2020, **31**, 4541–4551.
30 L. J. Chang, S. H. Luo, S. A. Li, X. S. Lang, X. Y. San, J. A. Liu and J. Z. Li, *Ionics*, 2020, **26**, 4977–4983.
31 C. Q. Shen, G. R. Li, L. Liu, P. F. Li, H. Xu, H. S. Hu and L. B. Wang, *J. Power Sources*, 2021, **496**, 229759.
32 R. T. Guo, H. L. Zhu and X. Y. Wang, *Int. J. Electrochem. Sci.*, 2022, **17**, 220758.
33 Z. L. Chen, Y. J. Gu, G. Y. Luo, Y. L. Huo and F. Z. Wu, *Ionics*, 2022, **28**, 191–200.
34 D. C. Fu, Q. Y. Cao, H. W. Song and C. X. Wang, *Chin. Sci. Bull.*, 2024, **69**, 2869–2882.
35 S. Kumar, P. Chand, A. Kumar and H. Anand, *Energy Nexus*, 2021, **1**, 100005.
36 S. Huo, B. Su, L. Chai, Y. Wang, L. Wang, M. Qi, T. Lai, Z. Liu, M. Li, A. Zhou, J. Qiu, W. Xue, H. Xu and X. He, *Energy Storage Mater.*, 2026, **84**, 104750.
37 Z. H. Zeng, H. Lei, J. X. Li, B. Wang, S. Y. Lei, X. B. Ji, W. Sun, Y. Yang and P. Ge, *Chem. Eng. J.*, 2024, **499**, 155616.